Geophysical Research Letters

RESEARCH LETTER
10.1029/2020GL090483

**Key Points:**

- 3D geodynamic models reveal that lithospheric buoyancy forces primarily drive ~E-W extension across East Africa
- Lithospheric buoyancy forces generate rigid plate motions aligned with kinematic predictions derived from GPS data
- Additional forces arising from horizontal mantle tractions may be required to explain along-rift surface motions in deforming zones

**Supporting Information:**

- Supporting Information S1

**Correspondence to:**
D. Sarah Stamps,
dstamps@vt.edu

**Citation:**
Rajaonarison, T. A., Stamps, D. S., & Naliboff, J. (2021). Role of lithospheric buoyancy forces in driving deformation in East Africa from 3D geodynamic modeling. *Geophysical Research Letters*, *48*, e2020GL090483. https://doi.org/10.1029/2020GL090483

Received 1 SEP 2020
Accepted 8 JAN 2021

# Role of Lithospheric Buoyancy Forces in Driving Deformation in East Africa From 3D Geodynamic Modeling

**Tahiry A. Rajaonarison**[1], **D. Sarah Stamps**[1], **and John Naliboff**[2,3]

[1]Department of Geosciences, Virginia Tech, Blacksburg, VA, USA, [2]Department of Earth and Environmental Sciences, New Mexico Tech, Socorro, NM, USA, [3]Department of Earth and Planetary Sciences, University of California, Davis, CA, USA

**Abstract** Despite decades of investigation, the origin of forces driving continental rifting remains highly debated. Deciphering their relative contributions is challenging due to the nonlinear and depth-dependent nature of lithospheric rheology. Recent geodynamic studies of the East African Rift (EAR) report contradicting results regarding the relative contribution of horizontal mantle tractions and lithospheric buoyancy forces. Here, we use high-resolution 3D regional numerical modeling of the EAR to isolate the contribution lithospheric buoyancy forces to observed deformation. Modeled surface velocities closely match kinematic models of the Somalian Plate, Victoria Block, and Rovuma Block motions, but provide poor fit to along-rift surface motions in deforming zones. These results suggest that lithospheric buoyancy forces primarily drive present-day ~E-W extension across the EAR, but intrarift deformation may result from viscous coupling to horizontal asthenospheric flow.

**Plain Language Summary** What forces drive continental rifting remains an outstanding question of geodynamics. Here, we investigate rifting along the East African Rift (EAR), which is the largest continental rift on Earth. Some studies suggest relatively shallow forces, known as lithospheric buoyancy forces, are thought to dominate the rifting. However, others suggest that deeper forces arising from interactions with mantle flow are driving the extension in the EAR. Here, we use advanced software to perform realistic 3D simulations to calculate the contribution of lithospheric buoyancy forces in driving the EAR. We find that lithospheric buoyancy forces are the primary driver of ~E-W rigid block motion across the EAR, whereas the deeper forces may be driving rift-parallel motions along the boundaries of rigid blocks. This result provides new insight into our understanding of how continents breakup.

## 1. Introduction

The East African Rift (EAR, Figure 1a) is the dominantly continental portion of the East African Rift System, which separates the Nubian and Somalian Plates and is the largest continental rift on Earth. The EAR is traditionally divided into three distinct rift segments: the northern EAR (Afar region), the Eastern Branch, and the Western Branch. Its spatial extent, heterogeneous lithospheric structure, and variable rates of extension across the EAR produce a wide range of deformation styles.

At present, the origin of forces driving extension across the EAR remains highly debated. The absence of regional slab-pull forces requires dominant contributions from lithospheric buoyancy and horizontal mantle flow. Lithospheric buoyancy arises from a combination of changes in lithospheric structure (composition, geothermal gradients) and surface topography (Fleitout, 1991; Fleitout & Froidevaux, 1982; Flesch et al., 2000; Jones et al., 1996), with the latter partially supported by vertical mantle flow (i.e., dynamic topography; Flesch et al., 2007). When isostatic compensation is assumed, lithospheric buoyancy can be quantified through the integration of lithostatic pressure to a compensation depth (i.e., gravitational potential energy ~GPE), with regions of locally high GPE undergoing extension (e.g., Coblentz & Sandiford, 1994).

While lithospheric buoyancy generates internal stresses driving deformation, mantle flow gives rise to both vertical and horizontal tractions acting at the base of the lithosphere (e.g., Bird, 1998; Bird et al., 2008; Coblentz et al., 1994; Koptev & Ershov, 2010; Lithgow-Bertelloni & Guynn, 2004; Naliboff et al., 2012; Yang & Gurnis, 2016). The magnitude of horizontal tractions acting on the base of the lithosphere is a function

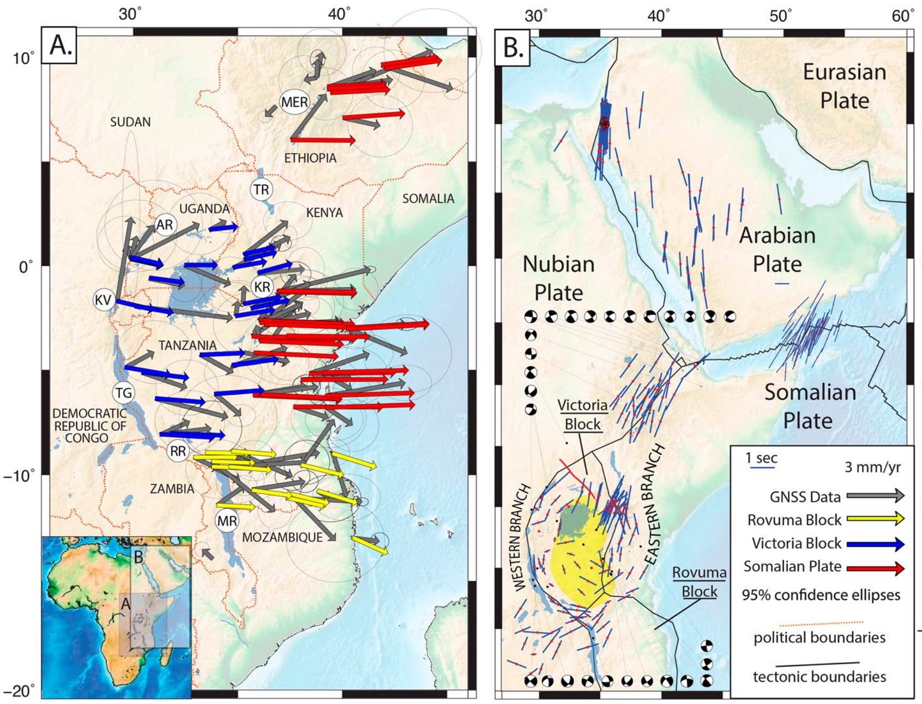

**Figure 1.** (a), GPS velocities along the East African Rift (EAR; Stamps et al., 2018; gray vectors with 95% confidence ellipses). Red, blue, and yellow vectors are kinematic models from Saria et al. (2014) for the Somalian Plate, the Victoria Block, and the Rovuma Block, respectively. Orange lines are political boundaries. Several rifts are defined: TG = Tanganyika Rift, RR = Rukwa Rift, AR = Albertine Rift, MER = Main Ethiopian Rift, TR = Turkana Rift, KR = Kenya Rift, MR = Malawi Rift, and KV = Kivu Rift. (b), Observed SKS splitting and strike-slip focal mechanisms along the EAR. The shear-wave splitting measurements are shown as blue bars with red circles showing the associated seismic station location. Black dots indicate earthquake locations where strike-slip focal mechanisms are observed (GCMT; Dziewonski et al., 1981; Ekström et al., 2012).

of both short- and long-wavelength convection patterns and the viscosity at the lithosphere-asthenosphere boundary, with deep and cold continental roots producing stronger coupling and higher stress magnitudes (e.g., Conrad & Lithgow-Bertelloni, 2006).

New GPS observations, combined with azimuthal seismic anisotropy and strike-slip focal mechanisms, provide insight into the balance of these two forces driving deformation across the EAR (Figures 1a and 1b). Several GPS stations positioned within rift segments measure nontransient secular surface motions between the Nubian and Somalian Plates that are rift-parallel, or oblique to the ~E-W extension across the broader rift system (Figure 1a). In particular, GPS velocities corrected for volcanic deformation in the Kivu Rift exhibit NNE trajectories (Ji et al., 2017; Stamps et al., 2018), while multiple GPS stations in the Eastern Branch and northern EAR exhibit a NE trend. In addition, strike-slip focal mechanisms within multiple rift segments (Figure 1b; Dziewonski et al., 1981; Ekström et al., 2012) provide evidence for strain partitioning reflecting rift-parallel deformation. N-S oriented azimuthal seismic anisotropy measurements beneath the Kenya Rift, Uganda, and Ethiopia (Figure 1b) likely reflects the northward mantle flow associated with the African Superplume (e.g., Bagley & Nyblade, 2013; Kendall et al., 2006). We hypothesize that the observed northward component of surface motions within rift segments may be the result of viscous coupling to northward mantle flow associated with a single plume (e.g., Bagley & Nyblade, 2013; Halldórsson et al., 2014; Kendall et al., 2006; Mulibo & Nyblade, 2013), or multiple plumes (e.g. Castillo et al., 2012; Chang & Van der Lee, 2011; Civiero et al., 2016; Furman et al., 2006; George et al., 1998; Lin et al., 2005; Nelson et al., 2008; Pik et al., 2006), and that the forces driving ~E-W opening of the Nubia-Somalia plate system are dominated by lithospheric buoyancy forces. Here, we use state-of-the-art 3D thermomechanical models of the EAR to isolate the contribution of lithospheric buoyancy to observed deformation patterns and test this hypothesis.

Prior studies of deformation within the EAR have been limited due to a lack of 3D thermomechanical modeling, although recent 3D thermomechanical experiments (Koptev, Burov, et al., 2018, Koptev, Calais, et al., 2018) suggest that the interactions of plumes with the lithosphere contribute to both rift initiation and evolution along parts of East Africa through lithospheric weakening and melt migration. Other 3D thermomechanical studies have also shown that inherited rheological weaknesses, such as shear zones, may play a role in producing the asymmetry of magmatism in the EAR (Koptev et al., 2016), and that strong cratonic blocks may be responsible for nonuniform splitting of plume materials beneath the central and southern EAR (Koptev, Cloetingh, et al., 2018). However, these studies do not address the distinct role of the lithospheric buoyancy forces in driving present-day deformation across the EAR. Furthermore, existing studies that examine the role of lithospheric buoyancy forces have relied on thin-sheet, or shell approximations, to model lithospheric deformation. While such approximations are computationally inexpensive and thus allow for conducting extensive sensitivity analyses, they fail to capture the nonlinear and depth-dependent nature of lithospheric rheology that affects transmission of both internal buoyancy forces and viscous coupling to horizontal mantle tractions (e.g., Coblentz & Sandiford, 1994; Min & Hou, 2018; Naliboff et al., 2012).

In this work, we characterize the contribution of lithospheric buoyancy forces in driving deformation across East Africa and surroundings, centered on the southern Eastern Branch. We developed a 3D regional model that comprises the lithosphere-asthenosphere system with topography imposed at the model surface and lateral density variations in the crust and mantle down to a compensation depth of 100 km. This model allows for estimates of surface motions to be solely driven by lithospheric buoyancy forces. To assess the contribution of lithospheric buoyancy forces to the present-day extension across East Africa, we compare several model outputs with previous modeling results (gravitational potential energy, geodetic strain rates, and surface motions from kinematic modeling) and GPS data.

## 2. Modeling Lithospheric Deformation of the East African Rift

We calculate dynamic velocities, continuous strain rates, and deformation style solely driven by lithospheric buoyancy forces for East Africa and surroundings. We use the open-source finite element code ASPECT (Bangerth et al., 2015, 2019; Kronbichler et al., 2012; Glerum et al., 2018; Naliboff et al., 2020) to model present-day (instantaneous) deformation driven by lithospheric buoyancy forces. The surface deformation is calculated by simulating a regional 3D thermomechanical model of the lithosphere-asthenosphere system that encompasses the EAR centered on the Eastern Branch. The model domain is 5,300 × 3,300 × 660 km in the East, North, and radial (depth) directions, consisting of upper, middle, and lower crustal layers, a mantle lithosphere layer, the asthenosphere, and the 410–660 km transition zone (Figure S1). We employ quadratic finite elements for the temperature fields, compositional fields, and velocity fields with a resolution of ~40 × 25 × 5 km. Our modeling approach includes the lithosphere, asthenosphere, and the transition zone down to 660 km depth, a nonlinear visco-plastic rheology, and initial conditions (temperature, density) constrained by synthetic lithospheric structure (Figure S3) based on average lithospheric thicknesses of the key tectonic regions derived from averages of the lithospheric models LITHO1.0 (Pasyanos et al., 2013), Fishwick (2010, updated), and an estimate of lithospheric thickness derived from shear wave tomography model from Emry et al. (2019). For cratonic regions (Tanzania Craton and Congo Craton) the lithospheric thickness is 150 km, 70 km for the Eastern Branch, 90 km for the Western Branch, and 100 km thick for mobile melts. We also impose 50 km thickness for oceanic ridges and 100 km thickness for oceanic lithosphere. The model is centered on the southern Eastern Branch such that the deforming regions are distant from the side boundaries to avoid boundary effects. The mechanical boundary conditions are free slip on all faces of the model, except at the bottom boundary, where it is fixed.

Crustal density variations are derived from CRUST1.0 (thicknesses and density for lower, middle, and upper crust; Figures S4 and S5; Laske et al., 2013) and ETOPO1 (Amante et al., 2009) data sets into the 3D model. The lithospheric temperature structure is a steady-state conductive geothermal gradient characteristic of the continental lithosphere (Chapman, 1986), which is constrained using estimates of regional lithospheric thickness and surface heat flow of the key tectonic regions (cratons, mobile belts, and rifts; Table S1). Following previous studies (e.g., Ghosh et al., 2009; Naliboff et al., 2012; Stamps et al., 2014), isostatic compensation is enforced through adjustments to the lithospheric mantle density (i.e., Pratt isostasy; Figure S6) down to 100 km, with a constant value of 3,300 kg/m$^3$ assigned from the compensation depth down to 660 km. We assume that all densities are independent of temperature. This approach allows for neglecting buoyancy driven mantle flow that might arise from plumes (e.g. Koptev, Burov, et al., 2018; Koptev, Calais, et al., 2018; Koptev, Cloetingh, et al., 2018) or lithospheric modulated convection (e.g., Njinju, Atekwana, et al., 2019; Rajaonarison, Stamps, Fishwick, et al., 2020) in the sublithospheric regions. While the geothermal gradient does vary within our model, temperature variations only affect the rheological structure. The rheological model of the crust combines nonlinear dislocation creep (dry quartzite; Gleason et al., 1995) with plastic failure. The mantle lithosphere rheological model follows olivine dislocation creep (Hirth & Kholstedt, 2003) combined also with plastic failure, while a composite rheology of dry olivine is used in the sublithospheric mantle (Jadamec & Billen, 2010). In the deforming regions, defined by Stamps et al. (2018), strain softening, which may arise from shear zones or faults that deform with frictional plasticity, is applied to promote strain localization (e.g., Brune & Autin, 2013; Huismans & Beaumont, 2003). The strain softening is implemented as a plastic strain weakening factor for cohesion and friction that reduces the lithospheric viscosity. Details of the numerical experiment, including the governing equation, the density variations, the initial temperature field, and the applied rheology, are described in the supplementary material Section S5.

## 3. Results and Discussion

### 3.1. Lithospheric Buoyancy Forces and Rift Strength

To provide a point of comparison with previous 2D studies of GPE-driven deformation in the EAR, we calculate regional GPE patterns using the lithostatic pressures from the 3D simulation. Following previous work that is consistent with our imposed isostatic compensation depth (e.g. Flesch et al., 2001; Ghosh et al., 2009; Jones et al., 1996; Stamps et al., 2014), we define GPE as the vertically integrated lithostatic pressure from a depth of 100 km to the surface and compare our results with Stamps et al. (2014). We chose a 100 km compensation depth because previous studies have shown that the inclusion of deeper density heterogeneities associated with cratonic roots produces minor effect on style and direction of lithospheric deviatoric stresses (e.g. Ghosh et al., 2009). Moreover, we have tested an isostatic compensation depth of 150 km, corresponding to the cratonic thicknesses, and found that the model produces less than a 2% increase in surface velocities indicating that GPE gradients in the EAR are contained in the upper 100 km and that our model is largely insensitive to compensation depths greater than 100 km.

The first-order patterns and magnitudes of the GPE from this study compare well with Stamps et al. (2014), which notably uses a lower resolution model of crustal thickness (CRUST2.0; Bassin, 2000) and topography (ETOPO5; Edwards, 1989, Figure 2a). Our modeled GPE distribution ranges from 1.52-1.66 TN/m in the African mainland to 1.40–1.52 TN/m in the oceanic basin (Figure 2b), whereas in Stamps et al. (2014) the same regions have values of 1.54–1.58 TN/m–1.46–1.52 TN/m. The residual between this study and Stamps et al. (2014) is between 0.05 and 0.1 TN/m (Figure 2c), which accounts for <10% of the total GPE and likely reflects variations in the assumed crustal structure and surface topography. Notably, the influence of surface topography is clearly evident in the shorter wavelength GPE variations observed in this study. However, given that the depth-integrated lithospheric buoyancy driving forces are similar to previous studies, the model design provides a template for analyzing the effects of vertically and laterally varying lithospheric structure on surface deformation patterns.

To test whether the available lithospheric buoyancy forces are capable of causing lithospheric rupture at the deforming zones, we consider six scenarios with variable lithospheric thickness and randomly reduced brittle strength (cohesion, friction) within the Eastern and Western Branches (Table S1). The reductions in brittle strength within the rift zones are achieved by applying an initial randomized plastic strain field between values of 0.5 and 1.5, over which the cohesion and angle of internal friction linearly weaken by a factor ($ø_{wf}$, Table S1). The imposed lithospheric thickness in the rifts varies by up to 20 km between models (Western Branch 80–100 km, Eastern Branch 60–80 km), which modifies the geothermal gradient and resulting viscosity in ductile portions of the lithosphere. For each simulation, the vertically integrated lithospheric strength is compared to the depth-averaged GPE, and the resulting plate and block rotations are compared with the kinematic predictions of Saria et al. (2014).

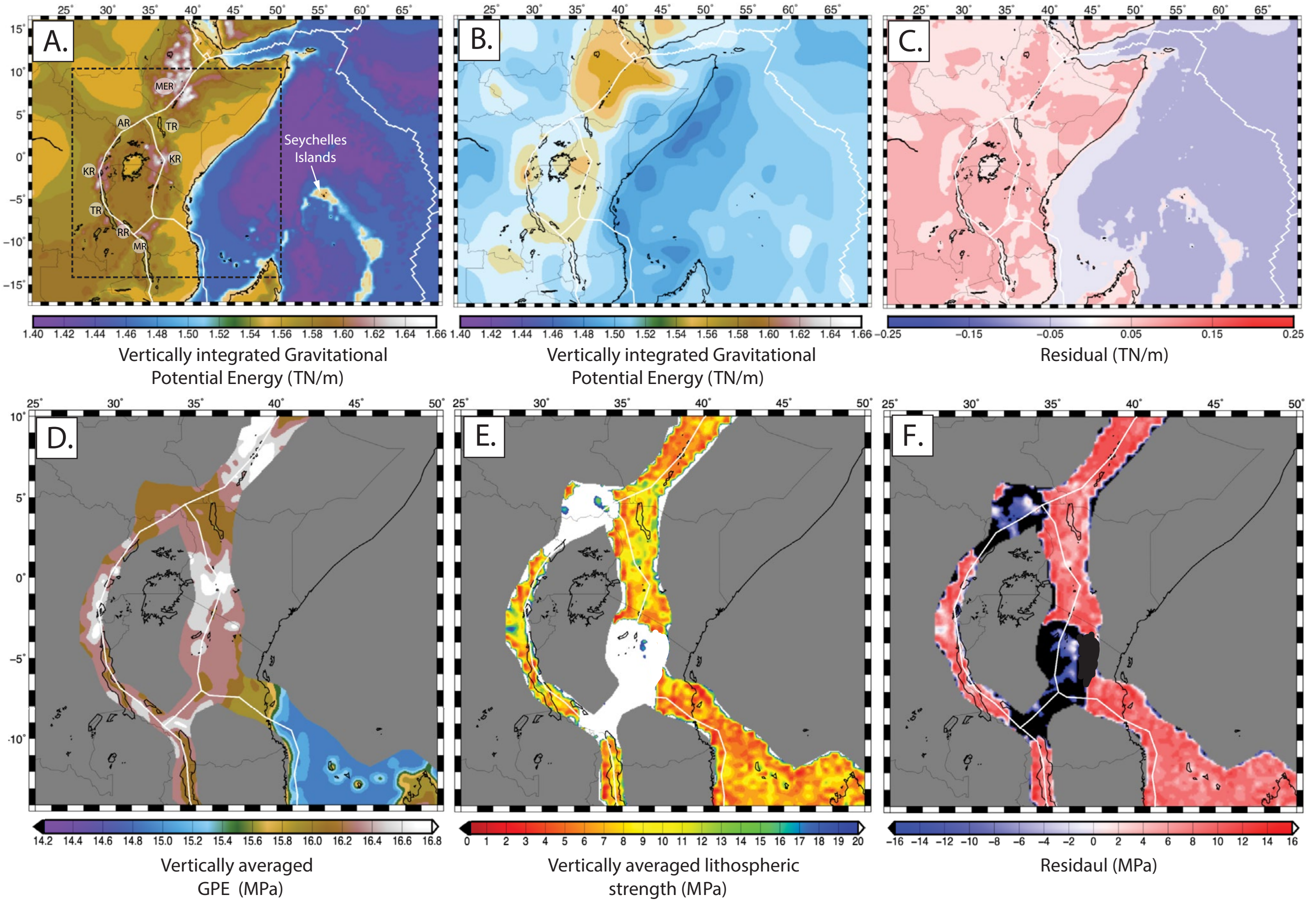

**Figure 2.** (a), Calculated GPE for the EAR from this study constrained by CRUST1.0 (Laske et al., 2012) and ETOPO1(Amante et al., 2009) topography data set with an isostatically compensated lithosphere of 100 km, from this study. Highest GPE are around the rifts. (b), GPE constrained by CRUST2.0 (Bassin, 2000) and ETOPO5 (Edwards, 1989) from Stamps et al. (2014) for an isostatically compensated lithosphere at 100 km depth. (c) The GPE residual between (a) and (b). Plate and block boundaries are from Stamps et al. (2018) (d), Vertically averaged GPE (averaged over 100 km) acting on the deforming regions of the EAR (e), Vertically averaged lithospheric strength for Model 1 (Table S1). (f), Residual between (d) and (e).

The available forces acting on the rifts are equal to the GPE averaged over 100 km, which ranges between 15.6 and 16.8 MPa (Figure 2d). For the case of intermediate rift lithospheric thicknesses (Western Branch ~90 km, Eastern Branch ~70 km), the available driving forces only exceed the lithospheric strength (Figure 2e) when the friction and cohesion are reduced by a factor of 0.01 (Model 1, Table S1). The excess of the available driving forces with respect to lithospheric strength is supported by the positive residual (Figure 2f). While rifting occurs in this case, reducing the brittle weakening factor sufficiently increases the lithospheric strength to prevent rifting and resulting plate velocities exhibit a poor fit to kinematic predictions (Models 2–3, Table S1).

While decreasing the lithospheric thickness by 10 km within both rift segments enables rifting to occur for brittle weakening factors of 0.1 and 0.01, both models (Models 4–5, Table S1) exhibit the worst fit to the kinematic predictions. Increasing the lithospheric thickness by 10 km and using a brittle weakening factor of 0.01 (Model 6) improves the RMS misfit significantly relative to Models 4 and 5, although the misfit values are roughly equivalent to Models 2 and 3 where rifting fails to occur. As Model 1 provides the best first-order match to the observations of plate motion, we hereby use it for analysis of individual regions.

### 3.2. Rigid Plate Rotation

To further test if lithospheric buoyancy forces drive present-day deformation across East Africa and surroundings, we compare our dynamic velocity estimates from our preferred model with kinematic predictions

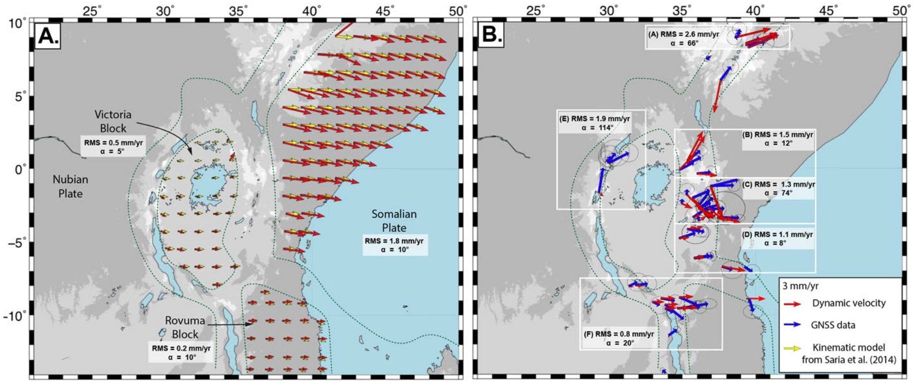

**Figure 3.** Surface velocities. (a), Dynamic velocities driven by variations in lithospheric buoyancy forces (red vectors) and kinematic predictions from the Saria et al. (2014) model (yellow vectors) within the Somalian Plate, the Victoria Block, and the Rovuma Block. (b), Dynamic velocities (red vectors) and GPS data from Stamps et al. (2018; blue vectors) within the deforming zones.

of surface motions within zones of rigidity (Saria et al., 2014, Figure 3a) and GPS velocities in intrarift zones (Stamps et al., 2018, Figure 3b). We also quantitatively compare the continuous strain rate magnitude (second invariant of strain rate) and qualitatively compare the style of deformation with the geodetic strain rate model of Stamps et al. (2018; Figure 4).

Surface velocities predicted by the block kinematic model of Saria et al. (2014) for the Somalian Plate, Victoria Block, and Rovuma Block are well reproduced by our dynamic velocities with an overall RMS misfit of

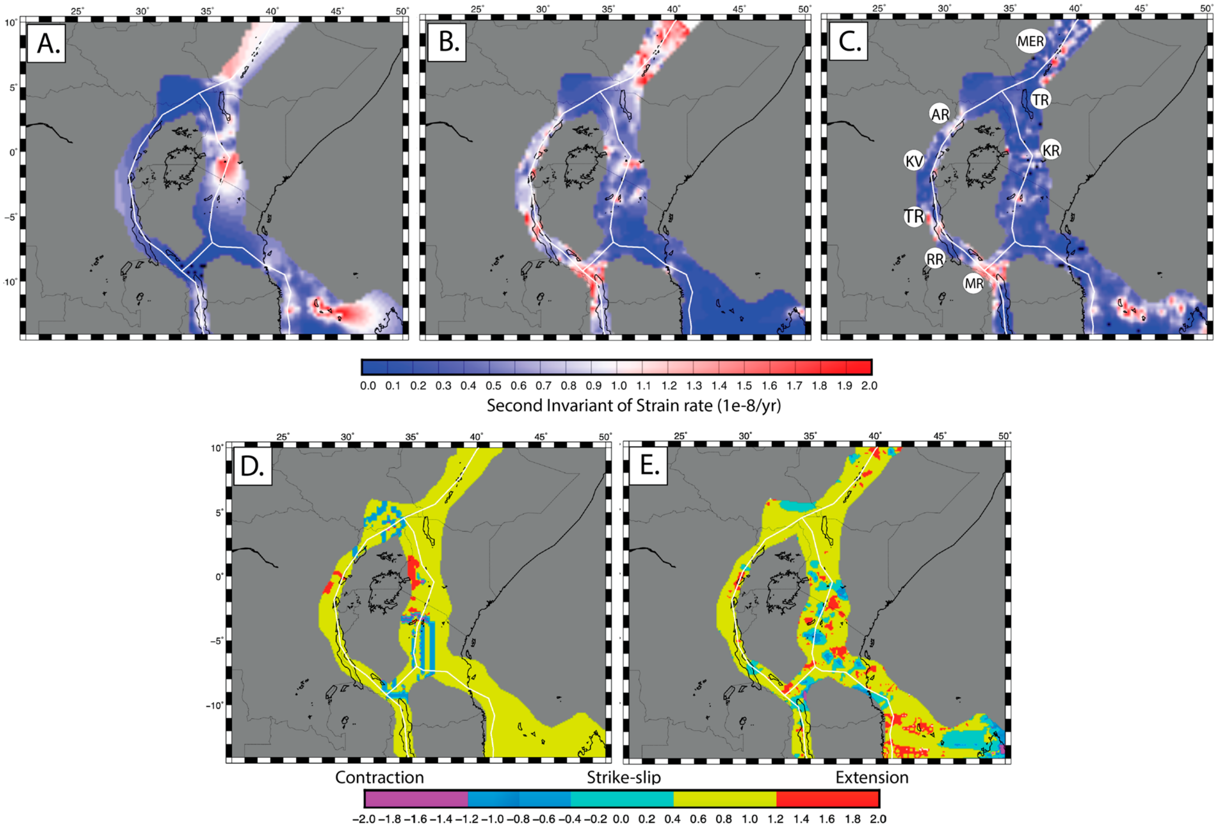

**Figure 4.** (a)–(c) Strain rate magnitude comparison: (a) Modeled vertically averaged dynamic strain rate magnitudes driven by lithospheric buoyancy variations, from this study, (b) geodetic strain rate magnitudes from Stamps et al. (2018). (c) Residual strain rate magnitudes. (d)–(f) Strain rate style comparison: (d) dynamic strain rate style, (f) geodetic strain rate style form Stamps et al. (2018).

1.4 mm/yr and angular misfit of 8° (Figure 3a). Since the dynamic velocities of the Nubian Plate are nearly zero, the velocities of the Somalian Plate, Victoria Block, and Rovuma Block can be regarded as in a Nubian-fixed reference frame. For the Somalian Plate, the dynamic velocities have a clockwise rotation at rates of ~2–6 mm/yr decreasing from north to south, while the kinematic velocities are slightly slower at ~2–5 mm/yr. The RMS value for the Somalian Plate in comparison with predicted velocities from Saria et al. (2014) is 1.8 mm/yr and the angular misfit is 10°. The clockwise rotation of the Rovuma Block in our region of study predicted by Saria et al. (2014) is on the order of 2 mm/yr and is consistent with our dynamic velocities with an RMS of 0.2 mm/yr and an angular misfit of 10°. For the Victoria Block, the dynamic velocity is ~1.4 mm/yr with a counterclockwise rotation decreasing from south to north, which is also consistent with the kinematic predictions. The RMS misfit is 0.5 mm/yr and the angular misfit is 5°.

As opposed to clockwise rotation of the Somalian Plate and the Rovuma Block with respect to Nubia, the counterclockwise rotation of the Victoria Block is an intriguing characteristic of the kinematics of the EAR (Fernandes et al., 2013; Glerum et al., 2020). However, many authors suggest contradicting explanations of its driving mechanism. Earlier studies attribute this counterclockwise rotation of the Victoria Block to plume-lithosphere interactions, with northward mantle flow pushing the keel of the Tanzania Craton positioned within the Victoria Block (Calais et al., 2006). Numerical models of Koptev et al. (2016) also reproduce the counterclockwise rotation of the Victoria block as a result of torque due to asymmetrically distributed forces exerted by plume material on the Tanzania Craton. However, in a more recent study, Glerum et al. (2020) used a numerical modeling approach to demonstrate that the rotation is due to edge-driven mechanisms caused by strong rheology at northernmost Western Branch and southernmost Eastern Branch. This new finding implies that lithospheric strength across the rifts control the rotation and only the far-field extensional forces are required. Our result is consistent with the edge-driven mechanism as our model incorporates the strong rheology at northernmost Western Branch and southernmost Eastern Branch where no plastic strain weakening is applied. Lithospheric buoyancy forces acting on laterally varying lithospheric strength causes the Victoria Block to rotate counterclockwise without the need for sublithospheric forces.

### 3.3. Intra-Rift Surface Motions

Overall, there is poor agreement between the dynamic velocities and GPS observations within the deforming zones (Figure 3b), with an overall RMS misfit of 2.9 mm/yr and angular misfit of 70°. In the Main Ethiopian Rift (Region A; Figure 3b), there is an alignment between the dynamic and GPS velocities at five stations and misalignment at three stations yielding a poor angular misfit of 66°. The dynamic velocities are twice as fast as the observations along the Main Ethiopian Rift with an RMS misfit of 2.6 mm/yr. The fit within the southern Eastern Branch is variable. Within the Kenya Rift, there is a good agreement in the northern segment (Region B; Figure 3b) with an RMS misfit of 1.5 mm/yr and angular misfit of 12°, but the fit worsens in the central segment (Region C; Figure 3b) where the dynamic velocities are oriented in the SE direction and the GPS velocities are oriented in the NE direction (RMS misfit of 1.3 mm/yr and angular misfit of 74°). In the southern segment of the Eastern Branch (Region D; Figure 3b), there is a good fit with GPS data with an RMS misfit of 1.1 mm/yr and angular misfit of 8°. In the central and northern Western Branch (Region E; Figure 3b; Kivu Rift and Albertine Rift), dynamic velocities are near zero, but the GPS velocities are up to 4 mm/yr and parallel to the rift with northward directions, yielding an RMS misfit of 2.1 mm/yr and angular misfit of 114°. For stations located in the Rukwa Rift and northern Malawi Rift, the dynamic velocities are mostly parallel to the ~E-W GPS velocity directions, but with lower magnitudes, yielding an RMS misfit of 0.8 mm/yr and angular misfit of 20°.

### 3.4. Strain Rates in Deforming Zones

For the comparison of vertically integrated strain rate magnitude through the lithosphere with the geodetic strain rate model of Stamps et al. (2018), we find that both models have similar patterns but slightly differ in magnitudes (Figure 4). Similar to the geodetic strain rate model, the estimated vertically integrated strain rate magnitude from our model is spatially varying across the rifts. The highest magnitudes ($0.9–1.3 \times 10^{-8}$ $yr^{-1}$, Figure 4a) are found in the Main Ethiopian Rift, which are slightly lower than the geodetic strain rate ($0.9–2.0 \times 10^{-8}$ $yr^{-1}$, Figure 4b), producing residuals between 0 and $2.0 \times 10^{-8}$ $yr^{-1}$ (Figure 4c). Along the Eastern Branch, our model predicts relatively large strain rate magnitudes of $1–2 \times 10^{-8}$ $yr^{-1}$ in the Kenya

Rift, but they are relatively low ($0.8–1 \times 10^{-8}$ yr$^{-1}$) in the Turkana Rift. In the Main Ethiopian Rift and the Eastern Branch, variations from high to low strain rates correspond to regions from high to low topography in this work. Along the Western Branch, the dynamic strain rates are mostly lower $0–0.8 \times 10^{-8}$ yr$^{-1}$ than the geodetic strain rates $0.8–2 \times 10^{-8}$ yr$^{-1}$. The highest residuals, ranging from 1.5 to $2 \times 10^{-8}$ yr$^{-1}$, between the dynamic strain rates and the geodetic strain rates are found along the Tanganyika Rift, the Rukwa Rift, and the northern Malawi Rift. The relatively low dynamic strain rates with respect to geodetic strain rates, along the Main Ethiopian Rift, in the central segment of the southern Eastern Branch, and along the Tanganyika Rift, the Rukwa Rift, and the northern Malawi Rift, indicate lithospheric buoyancy forces are not sufficient to produce the observed strain rate in the deforming zones of the EAR.

Predicted patterns of deformation style (compression, extension, strike-slip) patterns (Figure 4d) largely match those predicted by the geodetic strain rate model (Figure 4c). The deformation style exhibits dominantly extensional deformation with a component of strike-slip across the EAR, except at the northernmost Western Branch and the southernmost Eastern Branch where deformation is compressive. These regions of compression fall within imposed cratonic domains, which act as relatively rigid blocks due to the lower geothermal gradient and that plastic strain is not imposed. A minor difference occurs at the central segment of the Eastern Branch where the dynamic model predicts dominantly extensional deformation whereas the geodetic-based deformation style exhibits sparse regions of compressional deformation. This comparison of the predicted and geodetic deformation styles emphasize the predominance of the lithospheric buoyancy forces in driving E-W extension across the EAR.

## 4. Conclusions

Our 3D thermomechanical models of the EAR demonstrate that lithospheric buoyancy forces drive ~E-W extension across East Africa that results from rigid block rotation. These findings are consistent with previous 2D models of regional deformation patterns (i.e., Stamps et al., 2015), but contradict additional 2D studies that suggest horizontal tractions at the base of the lithosphere contribute significantly to observed large-scale deformation patterns across the EAR (Bird et al., 2008; Ghosh et al., 2013; Kendall & Lithgow-Bertelloni, 2016; Kusznir & Park, 1984). Our comparisons with intrarift GPS velocities demonstrate lithospheric buoyancy forces cannot explain all surface motions within the deforming zones. This work suggests that, across East Africa and surroundings, viscous coupling to horizontal mantle flow may play a role in driving deformation in regions that are relatively weak compared to rigid block rotations controlled by lithospheric buoyancy forces.

## Data Availability Statement

Most figures in this study have been generated with Generic Mapping Tools v5.4.2 (Wessel et al., 2013). One figure in 3D was created using the VISIT v2.9 software developed by the Lawrence Livermore National Laboratory. The ASPECT files needed to reproduce the model are achieved in Zenodo (Rajaonarison Stamps, & Naliboff, et al., 2020). In addition, the final model output files are archived at the Open Science Framework repository with doi https://doi.org/10.17605/OSF.IO/KSNB4 that are described in the supplementary information.

**Acknowledgments**
This work was funded by the National Science Foundation (NSF) GeoPRISMS grant EAR-1551864. The authors would like to thank the Computational Infrastructure for Geodynamics for supporting the development of ASPECT, which is funded by NSF Awards EAR-0949446 and EAR-1550901. They also thank Alexander Koptev for a constructure review that improved this manuscript.

## References

Amante, C., & Eakins, B. W. (2009). *ETOPO1 arc-minute global relief model: Procedures, data sources and analysis*. https://doi.org/10.7289/V5C8276M

Bagley, B., & Nyblade, A. A. (2013). Seismic anisotropy in eastern Africa, mantle flow, and the African superplume. *Geophysical Research Letters*, *40*, 1500–1505. https://doi.org/10.1002/grl.50315

Bangerth, W., Dannberg, J., Gassmoeller, R., Heister, T. (2019). *ASPECT v2.2.0 [software]*. zenodo. https://doi.org/10.5281/zenodo.3924604

Bangerth, W., & Heister, T. (2015). *ASPECT: Advanced solver for problems in Earth's convection* (pp. 1–571). Computational Infrastructure for Geodynamics.

Bassin, C. (2000). The current limits of resolution for surface wave tomography in North America. *Eos Transactions American Geophysical Union*, *81*, F897.

Bird, P. (1998). Testing hypotheses on plate-driving mechanisms with global lithosphere models including topography, thermal structure, and faults. *Journal of Geophysical Research*, *103*, 10115–10129. https://doi.org/10.1029/98JB00198

Bird, P., Liu, Z., & Rucker, W. K. (2008). Stresses that drive the plates from below: Definitions, computational path, model optimization, and error analysis. *Journal of Geophysical Research*, *113*. https://doi.org/10.1029/2007JB005460

Brune, S., & Autin, J. (2013). The rift to break-up evolution of the Gulf of Aden: Insights from 3D numerical lithospheric-scale modelling. *Tectonophysics*, *607*, 65–79. https://doi.org/10.1016/j.tecto.2013.06.029

Calais, E., Ebinger, C., Hartnady, C., & Nocquet, J. M. (2006). Kinematics of the East African Rift from GPS and earthquake slip vector data. *Geological Society, London, Special Publications*, *259*, 9–22.

Castillo, P. R., Hilton, D. R., Halldorsson, S. A., & Wang, R. (2012). The geochemical and Sr-Nd-Pb-He isotopic characterization of the mantle source of Rungwe Volcanic Province: Comparison with the Afar mantle domain. *AGUFM*, *2012*, T43C–2687.

Chang, S. J., & Van der Lee, S. (2011). Mantle plumes and associated flow beneath Arabia and East Africa. *Earth and Planetary Science Letters*, *302*, 448–454. https://doi.org/10.1016/j.epsl.2010.12.050

Chapman, D. (1986). Thermal gradients in the continental crust. *Geological Society, London, Special Publications*, *24*, 63–70. https://doi.org/10.1144/GSL.SP.1986.024.01.07

Civiero, C., Goes, S., Hammond, J. O., Fishwick, S., Ahmed, A., Ayele, A., & Leroy, S. (2016). Small-scale thermal upwellings under the northern East African Rift from S travel time tomography. *Journal of Geophysical Research: Solid Earth*, *121*, 7395–7408. https://doi.org/10.1002/2016JB013070

Coblentz, D. D., & Sandiford, M. (1994). Tectonic stresses in the African plate: Constraints on the ambient lithospheric stress state. *Geology*, *22*, 831–834. https://doi.org/10.1130/0091-7613(1994)022<0831:TSITAP>2.3.CO;2

Conrad, C. P., & Lithgow-Bertelloni, C. (2006). Influence of continental roots and asthenosphere on plate-mantle coupling. *Geophysical Research Letters*, *33*, L05312. https://doi.org/10.1029/2005GL025621

Dziewonski, A. M., Chou, T. A., & Woodhouse, J. H. (1981). Determination of earthquake source parameters from waveform data for studies of global and regional seismicity. *Journal of Geophysical Research*, *86*, 2825–2852. https://doi.org/10.1029/JB086iB04p02825

Edwards, M. O. (1989). Global gridded elevation and bathymetry (ETOPO5). *Global gridded elevation and bathymetry on 5-minute geographic grid (ETOPO5)*. Boulder, Colorado, USA: NOAA, National Geophysical Data Center.

Ekström, G., Nettles, M., & Dziewonski, A. (2012). The global CMT project 2004–2010: Centroid-moment tensors for 13,017 earthquakes. *Physics of the Earth and Planetary Interiors*, *200*, 1–9. https://doi.org/10.1016/j.pepi.2012.04.002

Emry, E. L., Shen, Y., Nyblade, A. A., Flinders, A., & Bao, X. (2019). Upper mantle earth structure in Africa from full-wave ambient noise tomography. *Geochemistry, Geophysics, Geosystems*, *20*, 120–147. https://doi.org/10.1029/2018GC007804

Fernandes, R. M. S., Miranda, J. M., Delvaux, D., Stamps, D. S., & Saria, E. (2013). Re-evaluation of the kinematics of Victoria Block using continuous GNSS data. *Geophysical Journal International*, *193*(1), 1–10. https://doi.org/10.1093/gji/ggs071

Fishwick, S. (2010). Surface wave tomography: Imaging of the lithosphere–asthenosphere boundary beneath central and southern Africa? *Lithos*, *120*, 63–73. https://doi.org/10.1016/j.lithos.2010.05.011

Fleitout, L. (1991). The sources of lithospheric tectonic stress. *Philosophical Transactions of the Royal Society of London*, *337*, 73–81. https://doi.org/10.1098/rsta.1991.0107

Fleitout, L., & Froidevaux, C. (1982). Tectonics and topography for a lithosphere containing density heterogeneities. *Tectonics*, *1*, 21–56. https://doi.org/10.1029/TC001i001p00021

Flesch, L. M., Haines, J. A., & Holt, W. E. (2001). Dynamics of the India-Eurasia collision zone. *Journal of Geophysical Research*, *106*, 16435–16460. https://doi.org/10.1029/2001JB000208

Flesch, L. M., Holt, W. E., Haines, A. J., & Shen-Tu, B. M. (2000). Dynamics of the Pacific-North American plate boundary in the western United States. *Science*, *287*, 834–836. https://doi.org/10.1126/science.287.5454.834

Flesch, L. M., Holt, W. E., Haines, A. J., Wen, L., & Shen-Tu, B. (2007). The dynamics of Western North America: Stress magnitudes and the relative role of gravitational potential energy, plate interaction at the boundary, and basal tractions. *Geophysical Journal International*, *169*, 866–896. https://doi.org/10.1111/j.1365-246X.2007.03274.x

Furman, T., Bryce, J., Rooney, T., Hanan, B., Yirgu, G., & Ayalew, D. (2006). Heads and tails: 30 million years of the Afar plume. *Geological Society, London, Special Publications*, *259*, 95–119. https://doi.org/10.1144/GSL.SP.2006.259.01.09

George, R., Rogers, N., & Kelley, S. (1998). Earliest magmatism in Ethiopia: Evidence for two mantle plumes in one flood basalt province. *Geology*, *26*. https://doi.org/10.1130/0091-7613(1998)026<0923:EMIEEF>2.3.CO;2

Ghosh, A., Holt, W. E., & Flesch, L. M. (2009). Contribution of gravitational potential energy differences to the global stress field. *Geophysical Journal International*, *179*(2), 787–812. https://doi.org/10.1111/j.1365-246X.2009.04326.x

Ghosh, A., Holt, W., & Wen, L. (2013). Predicting the lithospheric stress field and plate motions by joint modeling of lithosphere and mantle dynamics. *Journal of Geophysical Research*, *118*, 346–368. https://doi.org/10.1029/2012JB009516

Gleason, G. C., & Tullis, J. (1995). A flow law for dislocation creep of quartz aggregates determined with the molten salt cell. *Tectonophysics*, *472*, 213–225. https://doi.org/10.1016/0040-1951(95)00011-B

Glerum, A., Brune, S., Stamps, D. S., & Strecker, M. R. (2020). Victoria continental microplate dynamics controlled by the lithospheric strength distribution of the East African Rift. *Nature Communications*, *11*, 1–15. https://doi.org/10.1038/s41467-020-16176-x

Glerum, A., Thieulot, C., Fraters, M., Blom, C., & Spakman, W. (2018). Nonlinear viscoplasticity in ASPECT: Benchmarking and applications to subduction. *Solid Earth*, *9*, 267–294. https://doi.org/10.5194/se-9-267-2018

Halldórsson, S. A., Hilton, D. R., Scarsi, P., Abebe, T., & Hopp, J. (2014). A common mantle plume source beneath the entire East African Rift System revealed by coupled helium-neon systematics. *Geophysical Research Letters*, *41*, 2304–2311. https://doi.org/10.1002/2014GL059424

Hirth, G., & Kholstedt, D. (2003), Rheology of the upper mantle and mantle wedge: a view from the experimentalists. In J. Eiler (Ed.), *Inside the subduction factory* (138, pp. 83–105). American Geophysical Union.

Huismans, R. S., & Beaumont, C. (2003). Symmetric and asymmetric lithospheric extension: Relative effects of frictional-plastic and viscous strain softening. *Journal of Geophysical Research*, *108*(B10). https://doi.org/10.1029/2002JB002026

Jadamec, M. A., & Billen, M. I. (2010). Reconciling surface plate motions with rapid three-dimensional mantle flow around a slab edge. *Nature*, *465*, 338–341. https://doi.org/10.1038/nature09053

Ji, K. H., Stamps, D. S., Geirsson, H., Mashagiro, N., Syauswa, M., Kafudu, B., & d'Oreye, N. (2017). Deep magma accumulation at Nyamulagira volcano in 2011 detected by GNSS observations. *Journal of African Earth Sciences*, *134*, 824–830. https://doi.org/10.1016/j.jafrearsci.2016.06.006

Jones, C. H., Unruh, J. R., & Sonder, L. J. (1996). The role of gravitational potential energy in active deformation in the southwestern United States. *Nature*, *381*, 37–41.

Kendall, J.-M., & Lithgow-Bertelloni, C. (2016). Why is Africa rifting? *Geological Society, London, Special Publications*, *420*, 11–30. https://doi.org/10.1144/SP420.17

Kendall, J. M., Pilidou, S., Keir, D., Bastow, I. D., Stuart, G. W., & Ayele, A. (2006). Mantle upwellings, melt migration and the rifting of Africa: Insights from seismic anisotropy. *Geological Society, London, Special Publications*, *259*, 55–72. https://doi.org/10.1144/GSL.SP.2006.259.01.06

Koptev, A., Burov, E., Calais, E., Leroy, S., Gerya, T., Guillou-Frottier, L., & Cloetingh, S. (2016). Contrasted continental rifting via plume-craton interaction: Applications to Central East African Rift. *Geoscience Frontiers*, *7*, 221–236. https://doi.org/10.1016/j.gsf.2015.11.002

Koptev, A., Burov, E., Gerya, T., Le Pourhiet, L., Leroy, S., Calais, E., & Jolivet, L. (2018a). Plume-induced continental rifting and break-up in ultra-slow extension context: Insights from 3D numerical modeling. *Tectonophysics*, *746*, 121–137. https://doi.org/10.1016/j.tecto.2017.03.025

Koptev, A., Calais, E., Burov, E., Leroy, S., & Gerya, T. (2018b). Along-axis variations of rift width in a coupled lithosphere-mantle system, application to East Africa. *Geophysical Research Letters*, *45*, 5362–5370. https://doi.org/10.1029/2018GL077276

Koptev, A., Cloetingh, S., Gerya, T., Calais, E., & Leroy, S. (2018c). Non-uniform splitting of a single mantle plume by double cratonic roots: Insight into the origin of the central and southern East African rift system. *Terra Nova*, *30*, 125–134. https://doi.org/10.1111/ter.12317

Koptev, A. I., & Ershov, A. V. (2010). The role of the gravitational potential of the lithosphere in the formation of a global stress field. *Izvestiya - Physics of the Solid Earth*, *46*, 1080–1094. https://doi.org/10.1134/S1069351310120050

Kronbichler, M., Heister, T., & Bangerth, W. (2012). High accuracy mantle convection simulation through modern numerical methods. *Geophysical Journal International*, *191*, 12–29. https://doi.org/10.1111/j.1365-246X.2012.05609.x

Kusznir, N., & Park, R. (1984). Intraplate lithosphere deformation and the strength of the lithosphere. *Geophysical Journal International*, *79*(2), 513–538. https://doi.org/10.1111/j.1365-246X.1984.tb02238.x

Laske, G., Ma, Z., Masters, G., & Pasyanos, M. (2013). Update on CRUST1. 0—A 1-degree global model of Earth's crust. *In Geophysical Research Abstracts*. Vol. 15, (p. 2658).

Lin, S. C., Kuo, B. Y., Chiao, L. Y., & Van Keken, P. E. (2005). Thermal plume models and melt generation in East Africa: A dynamic modeling approach. *Earth and Planetary Science Letters*, *237*, 175–192. https://doi.org/10.1016/j.epsl.2005.04.049

Lithgow-Bertelloni, C., & Guynn, J. H. (2004). Origin of the lithospheric stress field. *Journal of Geophysical Research*, *109*. https://doi.org/10.1029/2003JB002467

Min, G., & Hou, G. (2018). Geodynamics of the East African Rift System ~30 Ma ago: A stress field model. *Journal of Geodynamics*, *117*, 1–11.

Mulibo, G. D., & Nyblade, A. A. (2013). Mantle transition zone thinning beneath eastern Africa: Evidence for a whole-mantle superplume structure. *Geophysical Research Letters*, *40*, 3562–3566.

Naliboff, J. B., Glerum, A., Brune, S., Péron-Pinvidic, G., & Wrona, T. (2020). Development of 3D rift heterogeneity through fault network evolution. *Geophysical Research Letters*, *47*. https://doi.org/10.1029/2019GL086611

Naliboff, J. B., Lithgow-Bertelloni, C., Ruff, L. J., & de Koker, N. (2012). The effects of lithospheric thickness and density structure on Earth's stress field. *Geophysical Journal International*, *188*, 1–17. https://doi.org/10.1111/j.1365-246X.2011.05248.x

Nelson, W. R., Furman, T., & Hanan, B. (2008). Sr, Nd, Pb and Hf evidence for two-plume mixing beneath the East African Rift System. *GeCAS*, *72*, A676. https://doi.org/10.1016/j.jog.2018.02.004

Njinju, E. A., Atekwana, E. A., Stamps, D. S., Abdelsalam, M. G., Atekwana, E. A., Mickus, K. L., et al. (2019a). Lithospheric structure of the Malawi Rift: Implications for magma-poor rifting processes. *Tectonics*, *38*, 3835–3853. https://doi.org/10.1029/2019TC005549

Pasyanos, M. E. (2013). A lithospheric attenuation model of North America. *Bulletin of the Seismological Society of America*, *103*, 3321–3333. https://doi.org/10.1785/0120130122

Pik, R., Marty, B., & Hilton, D. R. (2006). How many mantle plumes in Africa? The geochemical point of view. *Chemical Geology*, *226*, 100–114. https://doi.org/10.1016/j.chemgeo.2005.09.016

Rajaonarison, T. A., Stamps, D. S., Fishwick, S., Brune, S., Glerum, A., & Hu, J. (2020a). Numerical modeling of mantle flow beneath Madagascar to constrain upper mantle rheology beneath continental regions. *Journal of Geophysical Research. Solid Earth*, *125*, e2019JB018560. https://doi.org/10.1029/2019JB018560

Rajaonarison, T. A., Stamps, D. S., & Naliboff, J. (2020b). *Trajaona/aspect: Rifting model of the East African Rift (version v1.0)*. Zenodo. https://doi.org/10.5281/zenodo.4005094

Saria, E., Calais, E., Stamps, D., Delvaux, D., & Hartnady, C. (2014). Present-day kinematics of the east African Rift. *Journal of Geophysical Research: Solid Earth*, *119*, 3584–3600. https://doi.org/10.1002/2013JB010901

Stamps, D. S., Saria, E., & Kreemer, C. (2018). A geodetic strain rate model for the East African Rift System. *Scientific Reports*, *8*, 1–8. https://doi.org/10.1038/s41598-017-19097-w

Stamps, D., Flesch, L., Calais, E., & Ghosh, A. (2014). Current kinematics and dynamics of Africa and the East African Rift system. *Journal of Geophysical Research: Solid Earth*, *119*, 5161–5186. https://doi.org/10.1002/2013JB010717

Stamps, D., Iaffaldano, G., & Calais, E. (2015). Role of mantle flow in Nubia-Somalian plate divergence. *Geophysical Research Letters*, *42*, 290–296. https://doi.org/10.1002/2014GL062515

Wessel, P., Smith, W. H., Scharroo, R., Luis, J., & Wobbe, F. (2013). Generic mapping tools: improved version released, *Eos Transactions - American Geophysical Union*, *94*(45), 409–410. https://doi.org/10.1002/2013EO450001

Yang, T., & Gurnis, M. (2016). Dynamic topography, gravity and the role of lateral viscosity variations from inversion of global mantle flow. *Geophysical Supplements to the Monthly Notices of the Royal Astronomical Society*, *207*, 1186–1202. https://doi.org/10.1093/gji/ggw335